Graphene Oxide and Reduced Graphene Oxide: From Preparation to Verification of Safety and Therapeutic Efficacy in Silico And In Vitro

Pâmella Schramm Oliveira[a], Aline Rossato[b], Larissa da Silva Silveira[b], Cristian Mafra Ledur[b], Walter Paixão de Sousa Filho[b], Claudir Gabriel Kaufmann Junior[c], Sergio Roberto Mortari[b], Roberto Christ Vianna Santos[d], Guilherme Chagas Kurtz[e], Michele Rorato Sagrillo[b*], Cláudia Lange dos Santos[b].

[a] Graduate Program of Biomedical engineering, Universidade Franciscana - UFN, Santa Maria, Brazil.

[b]Graduate Program in Nanosciences, Universidade Franciscana - UFN, Santa Maria, RS, Brazil.

[c]Post Graduation Program in Mining, Metallurgical and Materials Engineering, PPGE3M, Universidade Federal do Rio Grande do Sul - UFRGS, Porto Alegre, RS, Brazil.

[d]Graduate Program of Pharmaceutical Sciences, Universidade Federal de Santa Maria - UFSM, Santa Maria, RS, Brazil.

[e]Computer Science, Universidade Franciscana – UFN, Santa Maria, RS, Brazil.

***Correspondence:** Dr. Michele Rorato Sagrillo, Program in Nanosciences, Universidade Franciscana, Santa Maria, RS, Brazil. E-mail: sagrillomr@ufn.edu.br

Abstract

To present a possible new alternative for wound treatment, this work evaluated the biological safety and therapeutic efficacy of graphene oxide (GO) and reduced graphene oxide (rGO) nanoparticles (NPs). First, the nanostructures were studied in silico and showed to be able to inhibit the production of some pro-inflammatory cytokines and stimulate the production of the anti-inflammatory cytokine IL-10, especially rGO. The results of the morphological and structural characterization of GO NPs synthesized from the Hummers method and reduced by ascorbic acid, were consistent with the literature, confirming their achievement. In the broth microdilution assay, GO and rGO showed antimicrobial activity against the clinical isolate of Streptococcus agalactiae (S. agalactiae) at a minimum inhibitory concentration (MIC) of 625 µg/mL for GO and 312.5 µg/mL for rGO. In addition, the nanostructure of rGO was able to inhibit, in subinhibitory concentration, the formation of S. agalactiae biofilm by up to 77% when compared to the positive control. Both NPs, in all tested concentrations, did not cause hemolysis, and alterations in coagulation in vitro assays. However, in the safety tests, it was evidenced that only the MIC of 312, µg/mL for rGO was biologically safe and presented anti-inflammatory and healing behavior in vitro. In general, the present work confirmed rGO's potential in the treatment of chronic wounds, since in silico showed anti-inflammatory behavior and in vitro showed therapeutic efficacy at low concentrations, prevented biofilm formation, and showed no significant toxic effects.

Keywords: Nanoparticles; Cicatrization; Anti-inflammatory; Antimicrobial.

1. INTRODUCTION

The healing process is determined by the initial characteristics of the wound, so the appropriate method of treatment should be chosen according to its ability to avoid hypoxia, infection, excessive edema, and foreign bodies. These factors create an environment that interrupts healing and thus produces a chronic wound (CHILDS and MURTHY, 2018). These late-healing wounds present high levels of pro-inflammatory cytokines (REINECKE et al., 2015) and pose serious risks to public health, as they affect a remarkable number of people, are at high risk of bacterial colonization, and are the main causes of limb amputation (AMBEKAR and KANDASUBRAMANIAN, 2019; DERAKHSHANDEH et al., 2018).

In infections, microorganisms can present themselves in the form of biofilm, which are aggregates of bacterial cells adhered to biotic and abiotic surfaces, incorporated in a self-produced extracellular matrix of exopolysaccharides (EPS), which hinders the action of antimicrobial agents (BJARNSHOLT, 2013; DONLAN and COSTERTON, 2002). Due to this, the formation of biofilm has become a challenge for the area of wound handling, as the bacteria that cause the infection cannot be effectively eradicated with the systemic administration of antibiotics and with topical applications of antimicrobial formulations (QIN, 2019).

Among the clinical methods of wound treatment, the most frequently used is the dressing. Although there is a variety of dressings and the pressure from the pharmaceutical industry to take up space in the market does not stop growing, there are still no ideal dressings (SMANIOTTO et al., 2010) i.e. that meet the requirements to be applied to all types of skin wounds.

Thus, aiming an improving of the quality of life of the population, there is a need to develop new materials, biologically safe, low cost, efficient against bacterial infections and the acceleration of chronic wound healing (THANGAVEL et al., 2018). In this area, treatment approaches using nanoscale (10^{-9} m) materials are interesting, due to the high surface area, biodegradability, and biocompatibility that helps in wound healing and the controlled release of drugs with combined effects (ZINE and SINHA, 2017). Furthermore, in nanotechnology, tools via computational simulations serve as a preliminary study, which analyzes the feasibility, creates two favorable biochemical interaction routes, and reduces the cost of in vitro and in vivo experiments. In this context, with a view to a possible new alternative for the treatment of wounds, in silico and in vitro studies of the biological properties of graphene oxide (GO) and reduced graphene oxide (rGO) nanoparticles (NPs) was carried out. Graphene-based materials present a high surface area, excellent electrical conductivity, good mechanical resistance, and high thermal conductivity. Moreover, they present good compatibility and can be easily operated with directional binders (CHUNG et al., 2013; THANGAVEL et al., 2018; YANG et al., 2013). The GO presents a two-dimensional structure formed by carbon atoms that are organized in a hexagonal structure functionalized by groups of oxygen such as epoxy, hydroxyl, and carboxyl (CHIU and HUANG and LAI, 2013; SINGH et al., 2018). The rGO, when compared to the GO, presents a decrease in electrical resistance and an increase in electronic conductivity, hydrophobicity, leaf aggregation, and the carbon/oxygen ratio due to the removal of the functional groups of oxygen from their leaves (CHUA and PUMERA, 2014; KUILA et al., 2013).

In recent studies, GO and rGO when combined with biopolymers, showed potential materials for wound treatment, as they showed good fluid uptake properties, angiogenic, antibacterial, anti-inflammatory,

and antioxidative (DIEZ-OREJAS et al., 2018; QIAN et al., 2018; THAMPI et al., 2017; THANGAVEL et al., 2018; ZINE and SINHA, 2017). Interestingly, in this area, the NPs of GO and rGO were hardly used pure, and thus, little is known about their biological properties and which nanostructure would be the most suitable for use in wound treatment. Based on this, this work aimed to produce, characterize, and verify the safety and therapeutic efficacy, as well as, the antimicrobial activity, antibiofilm, anti-inflammatory, and healing NPs of GO and rGO.

1. EXPERIMENTS

For the development of this work in silico (theoretical study) and in vitro (experimental studies) different methodologies were used, as presented in the flowchart of Figure 1.

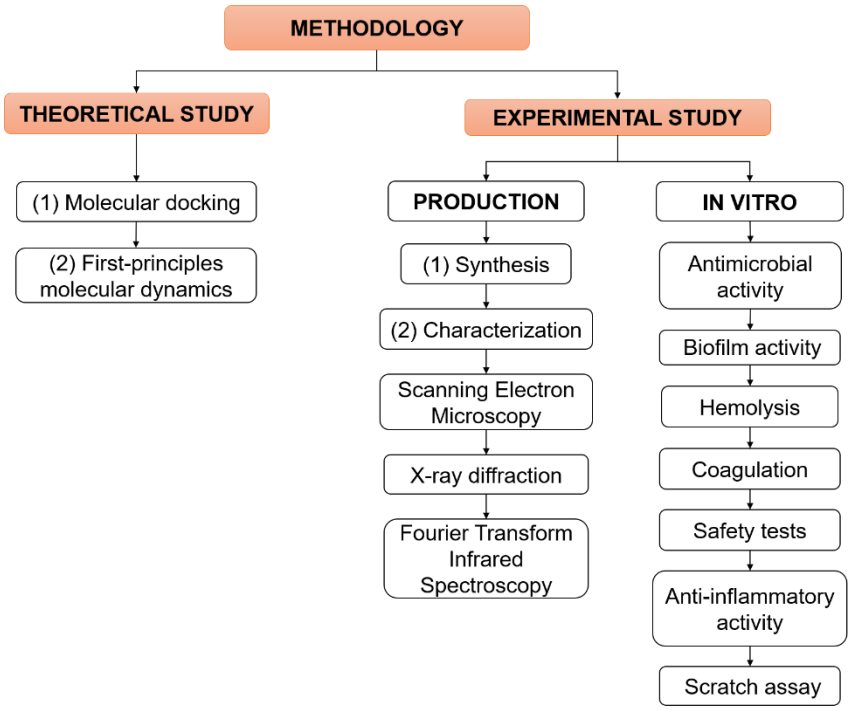

Figure 1. Methodologies used during this research.

1.1 In silico

2.1.1 Molecular docking

The study of molecular docking was performed through the AutoDock Vina® program, which consists of a set of open-source software that allows the modeling of structures, more specifically, provides the geometric and energetic 3D fit between a macromolecule (protein) and a small molecule (ligand) (TROTT and OLSON, 2009). Through this, the interaction between cytokines (IL-1, IL-6, IL-10, IL-15, INF-α, INF-γ, and TNF-α) and nanostructures (GO and rGO) was evaluated, to verify the affinity and the mode of connection between the referred systems.

The ligands (Figure 2a) were constructed according to the model proposed by Rosas et al. (2011) and their structures were converted to PDBQT format using AutoDockTools 4 software. The 3D structures of the inflammatory proteins (Figure 2b) were acquired in the PDB (Protein Data Bank) database (BERMAM et al., 2000) (IL-1 - PDB ID: 1G0Y; IL-6 - PDB ID: 1IL6; IL-10 - PDB ID: 2H24; IL-15 - PDB ID: 2Z3Q; INF-α - PDB

ID: 1ITF; INF-γ - PDB ID: 1EKU; TNF-α - PDB ID: 1TNF) and optimized in PyMol® and AutoDockTools 4 software. This process occurred by removing the ions and molecules from crystallographic waters, adding the hydrogen and partial charges, and files of proteins saved in PDBQT format.

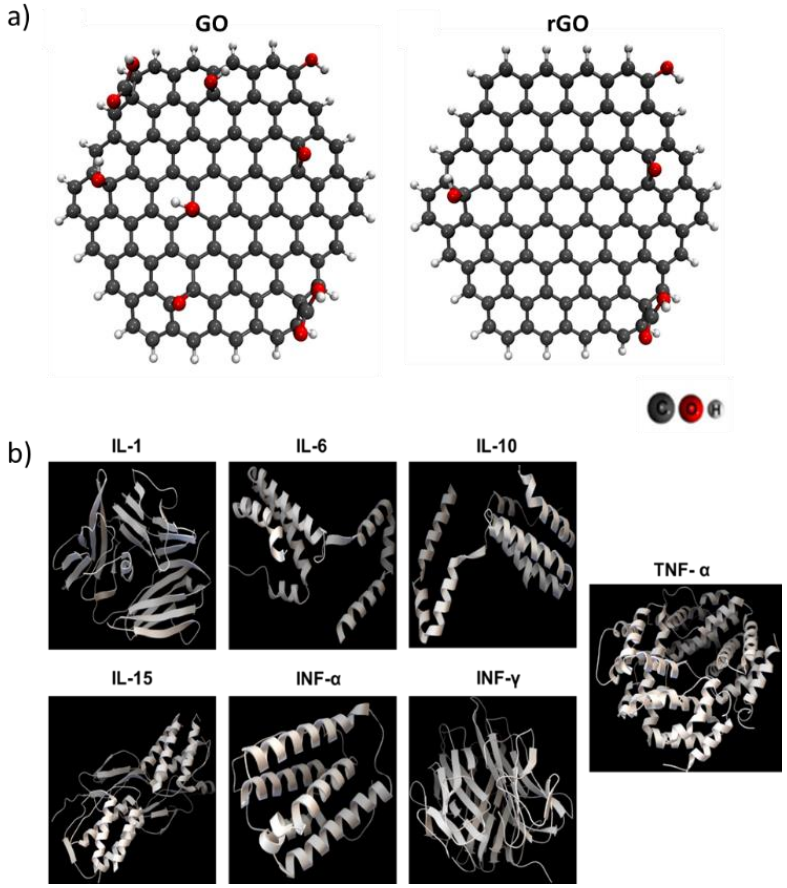

Figure 2. (a) Optimized molecular structures of the ligands and (b) 3D structures of the inflammatory proteins used. IL = Interleukin; TNF = Tumor necrosis factor; IFN = Interferon.

For the parameterization of the docking box, the values of the central coordinates were provided by the Deepsite® software (freely available at https://www.playmolecule.org), according to the active site of the proteins and are presented in Table 1 (JIMÉNEZ et al., 2017). The dimensions (Å) in x, y, z were calculated automatically by means of a script (available free of charge at https://www.brylinski.org/eboxsize), being [27.983; 27.983; 27.983] for GO and [27.895; 27.895; 27.895] for rGO (FEINSTEIN and BRYLINSKI, 2015). The Autodock Vina® software was executed to perform the molecular coupling, setting the parameter exhaustivity to 8 (FORLI et al., 2016). To model the complexes formed between proteins and binders, Free Energy of Binding (FEB) can be described as the Gibbs free energy (ΔG), which can be depicted as the sum of individual molecular-mechanics terms of standard-chemical potentials like van der Waals interactions (ΔG_{vdW}), hydrogen bonds (ΔG_H), electrostatic-interactions ($\Delta G_{electrost}$), and intra-molecular ligands interactions ($\Delta G_{internal}$), according to Eq. (1).

$$FEB \approx \Delta G(kcal/mol) = \Delta G_{vdW} + \Delta G_H + \Delta G_{electrost} + \Delta G_{internal} \quad (1)$$

The affinity values of FEB are classified as energetically unfavorable when the free energy of the protein-ligand complexes is ≥ 0 kcal/mol, indicating an extremely low or complete absence of affinity; otherwise, they are classified as the affinity of medium to high coupling (NISHIHIRA et al., 2019). O root mean square deviation (RMSD) was considered as a criterion of correct docking-pose accuracy with value < 2 Å and different from 0 Å (DURRUTHY et al., 2017), according to Eq. (2) (TROTT and OLSON, 2009; FORLI et al., 2016).

$$RMSD\left(pose_{i_{lig}}, pose_{i_{prot}}\right)(\text{Å}) = \sqrt{\frac{\Sigma_n(atom_{(i_{lig})} - atom_{(i_{prot})})^2}{n}} \quad (2)$$

where RMSD represents the mean of the distance between the atoms in a system, n the mean position of all the atoms in the system, and $atom_{(i_{lig})}$ and $atom_{(i_{prot})}$ the mean position of the atoms in the binder and the protein, respectively. Finally, the analysis of the non-covalent intermolecular interactions of the macromolecule-binding complex was carried out using 2D diagrams automatically plotted by the LigPlot v.4.5.3 software (LASKOWSKI and SWINDELLS, 2011).

Table 1. Center grid box.

PROTEIN	CENTER COORDINATE (Å) (x,y,z)
IL – 1	[27.6; 7.6; 141.1]
IL – 6	[2.8; -3.7; 4.9]
IL – 10	[18.9; 15.5, -17.5]
IL – 15	[55.4; 20.7; 5.1]
INF – α	[18.1; -37.3; 19.5]
INF – γ	[-4.4; 26.0; 32.6]
TNF – α	[9.4; 62.3; 32.7]

2.1.2 First-Principles calculations

The interaction of nanostructures with the amino acid groups of inflammatory proteins that have greater affinity was studied through first-principles calculations, a quantum approach based on the Density Functional Theory (DFT) (HOHENBERGA and KHON, 1964; KOHN and SHAM, 1965). The prediction of the properties of the interacting systems was performed using the SIESTA code (Spanish Initiative for Electronic Simulations with Thousands of Atoms), version 3.2 (SOLER et al., 2002). For the simulations, the interaction between the valence electrons and the ion core was described through conserved norm pseudopotentials (TROULLIER and MARTINS, 1991) and the exchange and correlation potential treated within the local density approximation (LDA) (CEPERLEY and ALDER, 1980). The Kohn Sham orbitals (KS) were expanded in double-ξ bases plus a polarization function (DZP). To ensure a good description of charge density, a cutoff of 300.0 Ry was used. The geometries of the studied systems were optimized until

the forces on the atoms were less than 0.05 eV/Å. For all calculations, an energy shift of 0.05 eV was used. As they are 0D systems, only one point k was used for the Brillouin zone integrations. We used a vacuum region of sufficient size to ensure neighboring cell systems did not interact. The binding energy was calculated according to equation (3), where E_{N+A} is the total energy of the interacting system (GO or rGO with amino acids); E_N is the total energy of GO or GOr and E_A is the total energy of the amino acid.

$$E_L = E_{N+A} - E_N - E_A \quad (3)$$

1.2 Experimental

2.2.1 Synthesis of NPs

The GO was produced by the Hummers method (HUMMERS and OFFEMAN, R., 1958) in an adaptation of Sun et al. (2008). In 1 g of graphite powder (Sigma-Aldrich, < 20 µm, Synthetic) 23 mL of concentrated H_2SO_4 (P.A., 95-98%, Synth) and 0.5 g of $NaNO_3$ (P.A., Merck) were added in a water bath under strong magnetic stirring at room temperature. Afterward, 3 g of $KMnO_4$ (P.A., Synth) was added, slowly, with mechanical agitation and in an ice bath (while the reagent was added), for 1H. Later, the material was kept in agitation, at room temperature for 96 h. After this time, 46 mL of distilled water was added, slowly, avoiding heating in the reaction medium (taking care that the temperature does not exceed 90°C). The mixture was kept in strong magnetic stirring for 15 min. The reaction was concluded by the addition of 140 mL of cooled deionized water and the addition of 10 mL of H_2O_2 (P.A., 30% v/v, Vetec), with mechanical stirring for another 10 min. The resulting material was filtered, washed with 250 mL of a 5% v/v HCl (P.A., Synth) solution to remove metal ions, and then was washed with distilled water countless times to remove the acid until it reached neutral pH. Before the drying step, the obtained solid was sonicated (Ultrasonic Bath, Elma, 150 W) for 30 min. Afterward, it was dried in the study at 60 °C for 24H. For storage and characterization, the GO was macerated and sieved in 325 mesh granulometry.

The rGO was obtained according to the methodology of Silva, Huang, and Yoshimura (2018), where a suspension of GO was prepared by sonication of 0.5 g of dry GO in 50 mL distilled water. In this, some drops of ammonium hydroxide (NH_4OH) were added, to adjust the pH. The suspension was kept in constant agitation at 65 °C for 1H. Later, the mixture of 50 mg of ascorbic acid ($C_6H_8O_6$) was added as a reducing agent. Afterward, the resulting material was washed several times and dried in a dissector.

2.2.2 Characterization of NPs

The Fourier Transform Infrared Spectroscopy (FTIR) test is important to verify the presence of functional groups of nanostructures. The equipment used was the PerkinElmer spectrometer, model Spectro One. For the preparation, the tablets were obtained with 2 mg of sample and 200 mg of support (Kbr).

The X-ray diffraction (XRD) provides information to identify the components present in the sample. This analysis was performed in the Bruker diffractometer, model D2 Phaser. The macerated samples were arranged in the sample holder in such a way that the surface is homogeneous. The analysis was performed in the range of 5° to 80°, with a pitch of 0.05064°/s, using copper anode (λ = 0.1540562 nm).

The analysis of morphology and size of the nanostructures obtained were done by Scanning Electron Microscopy (SEM), in the Sigma 300 VP model microscope (Carl Zeiss, England) with field emission

filament (FEG - Field Emission Gun) of the Schottky type (zirconium oxide coated tungsten filament), equipped with Gemini column (Zeiss, England).

2.2.3 Cell culture and treatments

In this study, the commercial lineage, HFF-1 ATCC ® SCRC- 1041™ (human fibroblasts) was used as well as lymphocytes and monocytes obtained from the collection of human peripheral blood, obtained through three samples of disposal from the Laboratory of Clinical Analysis of the Franciscan University, under the approval of the Ethics Committee on Human Beings of the Institution (CAAE: 31211214.4 .0000.5306) with no identification data.

After thawing, the lineages used were kept in polystyrene bottles in a culture medium according to the American Type Culture Collection, containing 10% bovine fetal serum (Invitrogen), 100 U/mL of penicillin (Invitrogen), and 100 U/mL of streptomycin (Invitrogen), in a humid atmosphere of 5% CO_2 at 37 °C. Upon reaching a satisfactory confluence, the cells were seeded in 96-well plates and treated with different concentrations of GO and rGO, and then incubated in an oven with times according to each cell assay.

2.2.4 In vitro assays

All in vitro experimental trials were performed in triplicate and treatments were used in serial dilution, from a 5,000 µg/mL standard solution. For the preparation of these solutions, the GO and rGO samples were solubilized in ultrapure water (Milli-Q ®) and later, with the help of an ultrasonic bath and vortex type agitator, the desired solubilization was achieved.

2.2.4.1 ANTIMICROBIAL AND ANTIBIOFILM ACTIVITIES

In the first phase of biofilm development (1 to 3 days), the cells are in a stationary phase within the microcolonies. Later, the maturation stage begins, which occurs the formation of micro and macro-colonies, together with the development of EPS (FALLATAH et al., 2019; MONDS and O'TOOLE, 2009). In this, the bacteria are active division or in exponential growth and are more susceptible to antimicrobials compared to bacteria in the stationary phase (FALLATAH et al., 2019; MASCIO; ALDER and SILVERMAN, 2007). Due to this, the time of 48 h of maturation was chosen for the realization of the antimicrobial tests and biofilms, because probably the cells divide more actively and become more vulnerable to NPs.

The antimicrobial activity of GO and rGO was evaluated by the technique of microdilution in the broth that determines the minimum inhibitory concentration (MIC) capable of causing inhibition of visible bacterial growth. This technique was performed according to Rossato et al. (2019), based on protocol M07-A8 of the Clinical & Laboratory Standards Institute (CLSI). Clinical isolates of *Pseudomonas aeruginosa* (*P. aeruginosa)*, *Streptococcus agalactiae* (*S. agalactiae)*, and *Multiple-resistant Staphylococcus aureus* (MRSA) from the Santa Maria University Hospital - RS, previously identified by specific phenotypic methods, were used. These were chosen because they are pathogenic invaders of chronic wounds, as well as biofilm-causing strains.

In the clinical isolate that presented antimicrobial activity, the capacity of biofilm formation in front of rGO was tested according to Stepanović et al. (2007). The test was performed in 96 polystyrene wells

plate, where 90 µL of Brain heart infusion broth (BHI) supplemented with 1% glucose, 20 µL of bactericidal inoculum, and 90 µL of subinhibitory concentration (sub-MIC) of the treatment was added. After incubation for 48 h at 37°C, the contents of the wells were discarded, and the plate was washed 3 consecutive times with 200 µL of sterile phosphate-buffered saline solution (PBS; pH 7.2) to remove all non-adherent cells and preserve the integrity of the biofilm. The fixation step occurred by adding 150 µL of methanol for 20 min. After the solution was discarded, and the plates dried at room temperature. The adherent layer formed in each well was stained with 150 µL of Hucker's 2% violet crystal solution for 15 min, followed by washing in running water. After the plate was dried, at room temperature, 150 µL of 95% ethanol was added to solubilize the biofilm. After 30 min at rest, the biofilm formation was revealed by reading the absorbances in a spectrophotometer with a wavelength of 570 nm.

2.2.4.2 HEMOLYSIS AND COAGULATION TEST

The hemolysis of GO and rGO was analyzed according to the methodology described by Dobrovolskaia et al. (2009), with treatments at different pH (7.2, 7.4, and 7.5). In this assay, PBS 1X pH 7.4 was added, proportionally to the blood volume (1:1), in the same heparin tubes (Vacuette®) used for blood collection and later these were slowly homogenized. Then they were centrifuged for 10 min at 1000 rpm and the supernatant was removed. This procedure was repeated (two times) (until a transparent supernatant was obtained). In Eppendorf microtubes containing 1 mL of PBS 1X, 50 µL of washed red blood cells were added and homogenized gently. Subsequently, 10 µL of treatment was added and samples were incubated for 1 h at room temperature. Then, they were centrifuged for 15 min at 1000 rpm and in a 96-well plate, 200 µL of the supernatant removed was added. The readings were performed in ELISA at a wavelength of 540 nm. In this test, red blood cells + PBS 1X were used as the negative control, and red blood cells + PBS 1X + DMSO or H2O were used as positives controls.

In the coagulation test, the tests were performed according to the Nanotechnology Characterization Laboratory protocol (Frederick National Cancer Research Laboratory, MD 21702). After collection, whole blood was centrifuged for 10 min at 2500 rpm. Subsequently, in a 96-well plate, 225 µL of plasma was added along with 25 µL of treatment and incubated at 37°C for 30 min. The reading was performed with Quick Timer II (Drake) coagulometer properly calibrated according to the manufacturer's recommendations for prothrombin time (PT) hemostasis (Labtest - batch: 4008) and activated partial thromboplastin time (APTT) hemostasis (Labtest - batch: 4006). The reference for the normal value of APTT was in the interval between 25 and 35 seconds, whereas the basal values for PT were in the interval between 12 and 15 seconds. These intervals were determined according to the literature (ADAMSON et al.,1993; SALVADOR-MORALES et al., 2009).

2.2.4.3 EVALUATION OF CELL VIABILITY

The test was performed according to Mosmann's method (MOSMANN, 1983) and for this purpose, when completing the incubation times of the cells, 20 µL of MTT solution (0.01M and pH 7.4) was added at a concentration of 5 mg/mL, diluted in PBS (phosphate buffer 1X). The plates receiving the solution were homogenized in the shaker and incubated for 2 hours at 37°C, protected from light, in an oven with 5% CO_2. Subsequently, the plates were centrifuged at 2000 rpm for 10 min. Then the supernatant was

removed from the wells and the cells were resuspended in 150 µL dimethylsulfoxide (DMSO). The absorbance is proportional to the number of viable cells and was determined by Elisa Anthos 2010 reader (Labtec, Austria) at a wavelength of 570 nm. In addition, the determination of cytotoxic potential was presented as a percentage to the negative control (cells in culture medium).

2.2.4.4 NITRIC OXIDE ASSAY

For the nitric oxide (NO) test, the sample used was the cell culture supernatant, where 50 µL of it was added to a new 96-well plate. Next, 50 µL of Griess' solution was added, composed by a solution I (Sulfanilamide 1%) + solution II (N-1-naftilethylenediamine 0.1%), in the ratio 1:1. The sample was kept in the dark at room temperature for 15 min. Finally, the absorbance was determined by an ELISA reader at a wavelength of 570 nm.

2.2.4.5 DICHLOROFLUORESCEIN DIACETATE ASSAY

For this technique, 96-well black plate was used, where 50 µL of the cell culture supernatant, 65 µL of Tris-HCl (10 mM, pH =7.4), and 10 µL of the 2.7-dichlorofluorescein diacetate reagent (DCFH-DA) were added. Subsequently, the plate was incubated for 1 h in the dark. The fluorescence reading was determined by Fluorimeter at 525 nm emission and 488 nm excitation.

2.2.4.6 FLUORIMETRIC DNA QUANTIFICATION ASSAY

The genotoxicity of GO and rGO was analyzed by a fluorometric assay of free extracellular double-stranded DNA (dsDNA) quantification in the medium due to cellular apoptosis. For this, the reagent PicoGreen® was used, a fluorescent dye capable of binding to dsDNA (COSSETIN et al., 2019). For the assay, a 96-well black plate was used, where 10 µL of the cell culture supernatant, 80 µL of TE 1X (Tris HCl 10 mM and EDTA 1 mM pH=7.5), and 10 µL of the PicoGreen® DNA reagent (Life Technologies) were added. Subsequently, the plate was incubated for 1 h in the dark. The fluorescence reading was performed on the spectrofluorometer at 480 nm (excitation) and 520 nm (emission) (SAGRILLO et al., 2015).

2.2.4.7 ANTI-INFLAMMATORY ACTIVITY

The monocytes were plated on a 96-well plate (Corning Inc., Corning, NY, USA) and after 24 hours of incubation, the treatment was initiated with 50 µL of phytohemagglutinin (PHA) and rGO at a concentration of 312.5 µg/mL. The cells remained in an oven for 48 h at 37° C with 5% CO_2 (MACZYNSKI et al., 2016), then the plate was centrifuged, and the supernatant was removed for MTT and NO tests. As a negative control, the culture of untreated cells with PHA was used and as a positive control, the cells were stimulated with hydrogen peroxide (H_2O_2).

2.2.4.8 SCRATCH ASSAY

This experiment was performed according to the methodology proposed by Riéffel (2019), with some modifications. The culture conditions were optimized to ensure that the cell monolayers were homogeneous, maintaining cell viability before the injury. To reduced cell proliferation, the fibroblast cell

lines grew until they reached confluence in a 96-well plate. Initially, the culture medium was removed, and with the tip of a sterile needle, a continuous cut was simulated on the medial surface of each well to analyze the cellular migration to the wound region. Later, the cells were washed with PBS (Gibco®), composed of sodium chloride and sodium phosphate, for the removal of cell debris. The wound closure was monitored by digital photographs taken under a microscope at the time of cutting and after 24 and 48 h.

Figure 3 presents the step-by-step of the test, and for the data analysis step a script was developed in the Python programming language, where initially images of size 50x50 pixels were generated, representing a sample of cells, i.e., a fully healed region. From this image, the average and standard deviation of the color of its pixels were calculated in RGB (Red, Green, and Blue) format, whose values for each color vary from 0 to 255. From the calculated mean, the analysis of the healing process of the images was started, analyzing them pixel by pixel. The color of a pixel was considered as a cell if its RGB value is greater than or equal to the mean minus the standard deviation, or less than or equal to the mean plus the standard deviation. Otherwise, the pixel was considered as non-cell. Thus, it was calculated how many pixels of each image are within the cell and non-cell range, as well as the cell and non-cell percentages about the total amount of pixels. Finally, a file was generated by the script, in a table format, in which the data referring to the percentage of cells present at the cut location were used for the comparison of healing between the control and rGO samples.

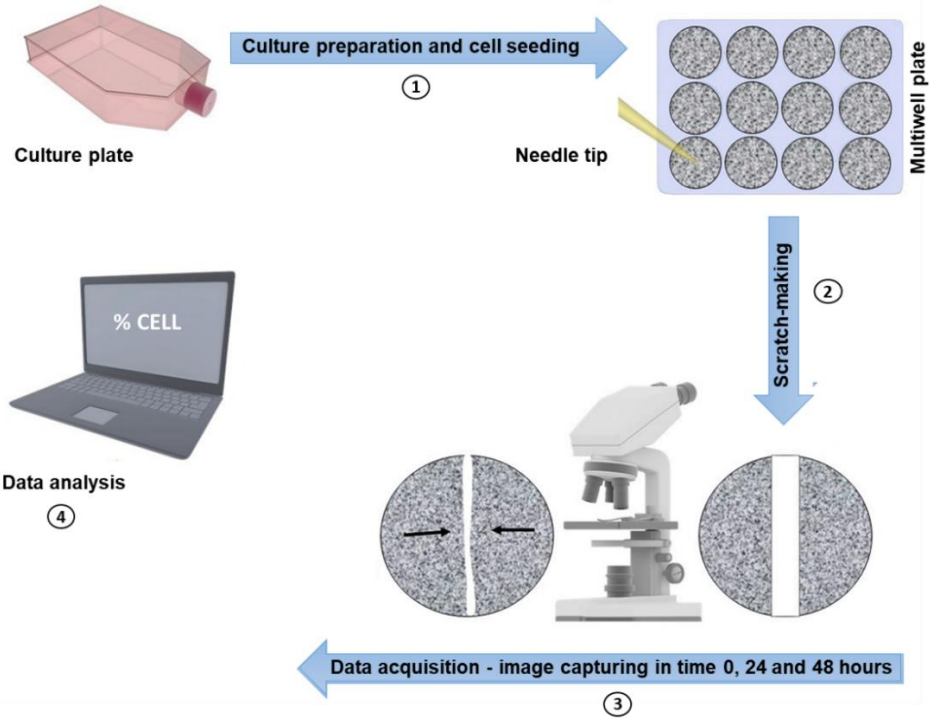

Figure 3. In vitro healing test steps (adapted Grada et al. (2017)).

1.3 Statistical analysis

The results of hemolysis and cytotoxicity were presented as a percentage of the untreated control group (negative control). The analyses were performed using a one-way bilateral analysis of variance (ANOVA) followed by Dunnett's post hoc test. Values with $p < 0.05$ were considered statistically significant. The data were expressed as mean ± standard deviation. The graphs were prepared using GraphPadPrism version 5.01 (GraphPad Software, La Jolla, CA, USA).

The OD readings obtained in the biofilm formation assay were recorded as mean ± standard deviation (SD) and bilateral one-way ANOVA followed by Dunnett's post hoc test. Values with $p < 0.05$ were considered statistically significant. The graphs were prepared using GraphPadPrism version 5.01 (GraphPad Software, La Jolla, CA, USA).

2. RESULTS AND DISCUSSION

2.1 In silico study

3.1.1 Molecular docking

The docking protein-binding allows an analysis of the favorable biochemical interactions and thus predicts whether the binding substance will potentially bind to the receptor (protein) in vitro or in vivo. This study was performed in AutoDockTools 4 software, and the results of the best complexation settings are present in Table 2.

Table 2. Affinity and RMSD values for the best fitting configurations of each system studied.

LIGAND	PROTEIN	FEB (kcal/mol)	RMSD (Å)
	IL – 1	-11	1.507
	IL – 6	-4	1.566
	IL – 10	**-13.8**	**1.68**
GO +	IL – 15	-8.8	1.187
	INF – α	-9.4	1.759
	INF – γ	-9.2	1.85
	TNF – α	**162.2**	**0**
	IL – 1	-12.5	1.035
	IL – 6	-3.8	1.629
	IL – 10	**-15.5**	**1.08**
rGO +	IL – 15	-11	1.468
	INF – α	-10.1	1.608
	INF – γ	**-9.7**	**12.742**
	TNF – α	**181.3**	**4.369**

According to the results found, there is an absence of affinity in the rGO-INF-γ complex and between both binding agents and the TNF-α protein. On the other hand, the weakest interactions occur in the rGO-IL-6 and GO-IL-6 complexes of FEB -3.8 and -4 kcal/mol, respectively. Thus, it is observed that the structures

that presented little or no affinity with GO and rGO are pro-inflammatory proteins, which can prolong the inflammatory phase during the wound healing process.

The FEB value of the rGO-IL-10 complex was the most negative interaction energy (-15.5 kcal/mol), thus being the strongest interaction when compared to the other systems that presented molecular affinity. The second best coupling also occurred with the IL-10 protein (GO-IL-10 complex; FEB= -13.8 kcal/mol), probably due to the interaction of the studied graphene derivatives being stronger with anti-inflammatory proteins, thus reinforcing the healing potential of these nanostructures.

The most favorable complex (Fig. 4a) presented hydrophobic contact interactions and hydrogen bonding (more intense intermolecular force) between the rGO carboxyl group and the Glu142 residue. In this bond, the interatomic distance was 2.84 Å, that is, < 7 Å which is considered relevant for the coupling process between the systems in molecular docking (DURRUTHY et al., 2017). Moreover, this interaction occurred with the amino acid glutamine (Glu), which is an important energy source for all cells of the immune system, being very beneficial in immune function, especially concerning the proliferation of defense cells (SOUSA et al., 2015).

The 2D diagram of the second coupling with higher affinity (Fig. 4b) presented only hydrophobic contact interactions (between non-polar groups) and, although these are considered relatively weak interactions when compared to the others, they are of great relevance in the process of complexation with a protein. Moreover, as chemical bonds are not present, the high affinity of this complex occurred possibly by the process of physical adsorption, and this will be better understood in the next phase of the study in silico (first principles calculations).

Briefly, in the molecular docking, the studied nanostructures showed that they would be able to inhibit the production of some pro-inflammatory cytokines and stimulate the production of the anti-inflammatory cytokine IL-10. Therefore, due to the participation of cytokines in directing the immune response and activation of mononuclear leukocytes, fundamental for the development of inflammatory response (AVELAR et al., 2011; CAPELARI-OLIVEIRA et al., 2011; PREETHI ; KUTTAN and KUTTAN, 2009), the identification of anti-inflammatory and immunosuppressive properties in silico represents a promising strategy for the development of healing materials using GO and rGO.

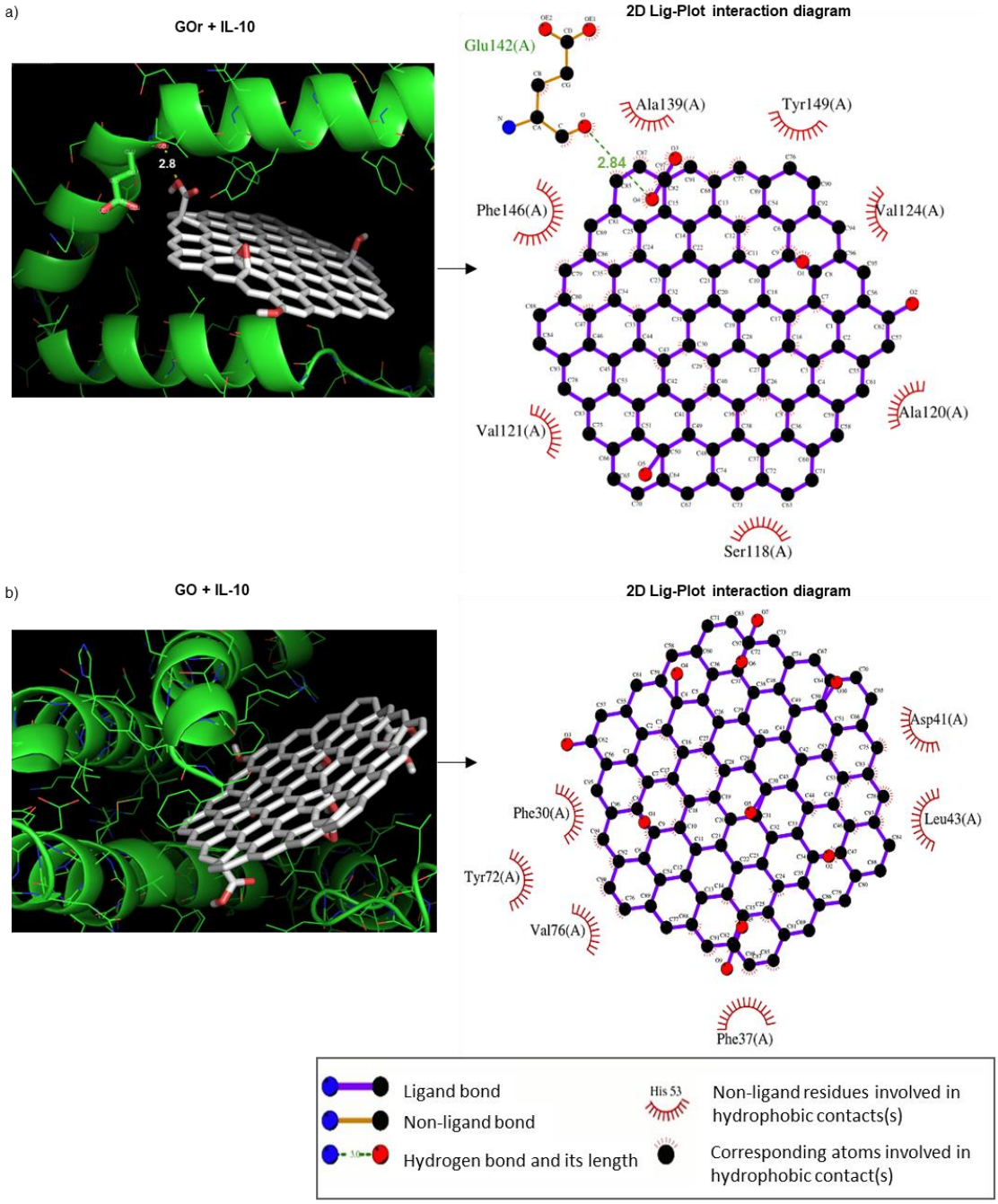

Figure 4. (a) 3D representation of the best fit configuration and 2D diagram of the type of interaction of the coupling with higher affinity (rGO-IL-10 complex) and (b) second coupling with higher affinity (GO-IL-10 complex).

3.1.1 First-Principles Calculations

Based on the results of the molecular docking calculations, first-principles calculations were performed for the configurations that resulted in better coupling. For the interaction with GO, the amino acids tested were those that have a hydrophobic contact, i.e., the amino acids aspartic acid, phenylalanine, leucine, tyrosine, and valine. As for the interaction with rGO, only hydrogen bonding with the amino acid glutamic acid was studied. The interaction configurations of the studied systems are shown in Figure 5.

Table 3 shows the main results of the interactions studied, i.e. the smallest distances between the atoms of GO /GOr and amino acids and the binding energy of the interacting system.

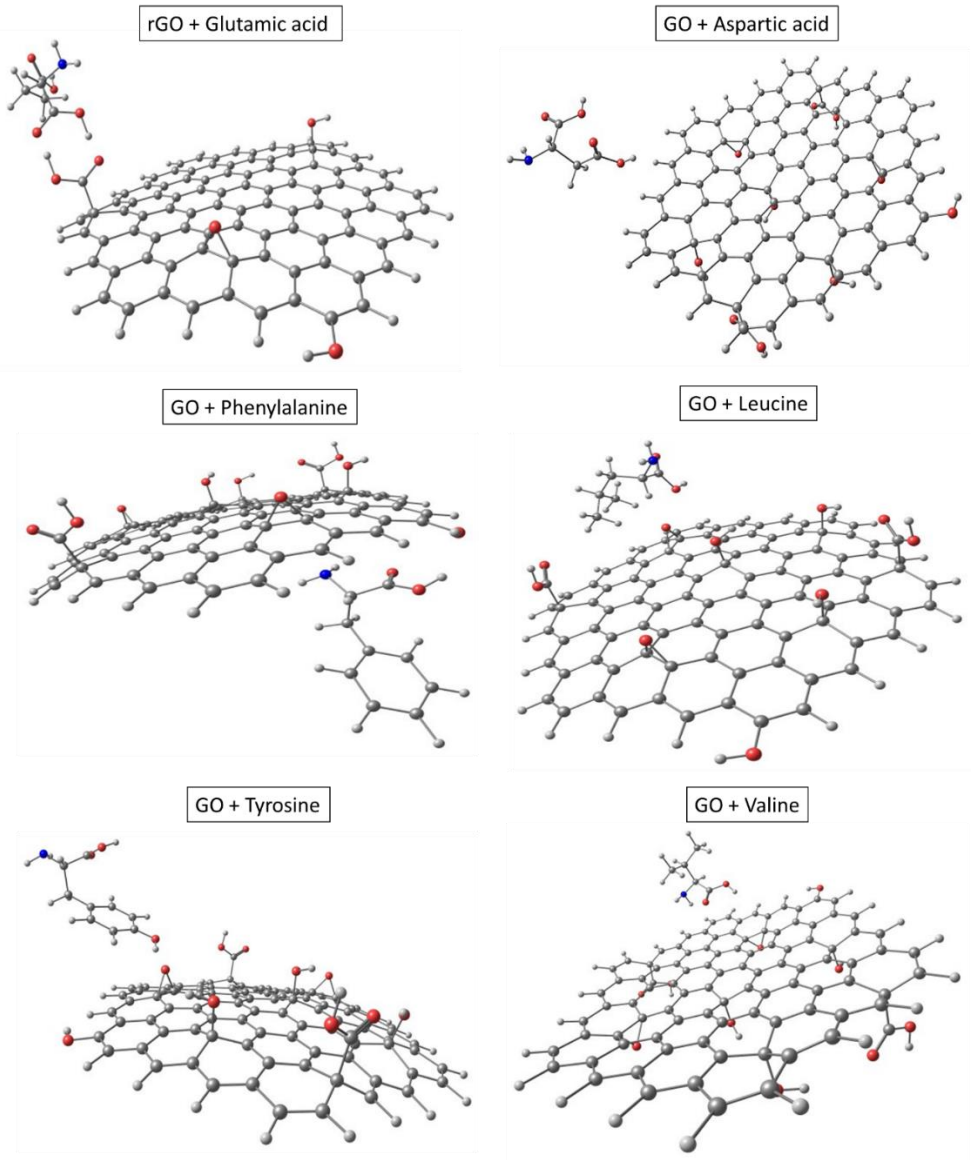

Figure 5. Configurations of GO interactions with amino acids: phenylalanine (A), leucine (B), tyrosine (C) and valine (D).

As shown in Table 3, the binding energy of the system GO + aspartic acid corresponds to an unfavorable system (eV > 0), while the other energies of the studied systems against GO range from -0.420 to -1.012 eV. From the characteristics of the interactions and the energy values, it can be concluded that they are physical interactions, i.e, there is a weak interaction between the interacting systems. Since the higher, the binding energy (in modulus), the more stable the configuration, the most stable and most likely to be preserved is the interaction between GO and phenylalanine.

Based on the interaction of rGO with glutamic acid, we can observe that the binding energy is the highest among the studied systems (-1.65 eV). Moreover, the distance between the nearest atoms of rGO and

the amino acid is only 1.23 Å. This behavior is consistent with a chemical interaction, i.e. there is a strong bond between rGO and glutamic acid.

These results show that both GO and rGO interact with the amino acids studied. However, the most important result is the strong interaction with rGO, which shows that this particular nanomaterial would be a promising candidate for the present work proposal.

Table 3. Distances between atoms of GO /rGO and nearest amino acids and binding energy of interacting systems.

CONFIGURATION		DISTANCE (Å)	BINDING
LIGAND	AMINO ACID		ENERGIES (eV)
	Aspartic acid (Asp41)	2,22	2,740
	Phenylalanine (Phe30)	1,99	**-1,012**
GO	Leucine (Leu43)	2,10	-0,530
	Tyrosine (Tyr72)	1,62	-0,767
	Valine (Val76)	2,17	-0,420
rGO	Glutamic acid (Glu142)	1,23	**-1,654**

2.2 Experimental study

3.2.1 Preparation and characterization of nanostructured

The production of the nanostructures was first achieved by obtaining GO from graphite oxidation synthesis, followed by reduction by ascorbic acid, resulting in rGO with a yield of approximately 80%. All samples were obtained in scattered and fine black powder (Fig. 6a) and the images acquired by GO SEM in different magnifications (Fig. 6b and c) allowed their morphological characterization. Micrography confirms the nature of GO by the typical ripples present on its surface due to successful graphite exfoliation (WANG and CHEN and CHEN, 2014).

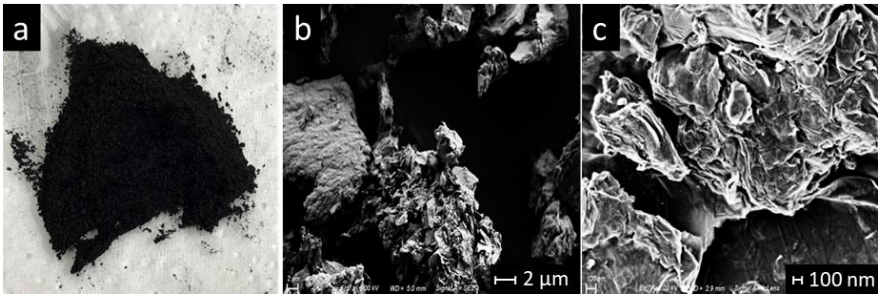

Figure 6. Photographic image of the characteristic nanostructures powder (a); Micrographs (SEM) of GO in 5,000 X (b) and 90,000 X (c).

The diffractograms of the starting graphite and the nanostructures produced are represented in Figure 7a, respectively. The XRD test identified characteristic graphite peaks, such as 2θ = ~26° (002) and 55°, which correspond to the standard diffraction chart number 9012230 of Crystallography Open Database - DOC.

In Figure 7b, the high efficiency of GO production is evidenced by the disappearance of the sharpest graphite peak and the new diffraction peak around 2θ = 10°, which indicates a phase with a greater interplanar distance (KRISHNAMOORTHY et al., 2013; SHEN et al., 2009) due to the presence of functional groups of oxygen and water molecules in the carbon layer structure (SIBURIAN et al.,2018). In the rGO diffractometer, the displacement of the peak (002) is observed indicating that there was a reduction in the number of functional groups on the surface of the graphene sheets (FARIA et al., 2017). Moreover, in both nanostructures there is the formation of a lower intensity peak around 2θ = 42.6°, corresponding to the plane (100) of the hexagonal carbon structure (KIM et al., 2016).

The analyses of the chemical groupings present in the GO and rGO samples were performed through FTIR (Figure 7c). In the absorbance spectrum, it was verified the presence of an enlarged band in GO, between 2950 and 3500 cm^{-1}, assigned to the -OH groupings. The low-intensity band marked around 1725 cm^{-1} refers to the carboxylic groups of both nanostructures (CORDEIRO, 2018), while the intense peak around 1550 cm^{-1} refers to the aromatic groups C=C of rGO (DORFEY and MORTARI and VOLKMER 2017; WANG and SALIHI and ŠILLER, 2017). The peaks around 1400 cm^{-1} are associated with bending modes in C-(C=O)-C groups and the bands centered at 1025 cm^{-1} refer to the symmetric vibrations between carbon and oxygen atoms in C-O groups. Also, the bands of the region from 600 to 900 cm^{-1} of GO are attributed to the C-O binding modes of hydroxyl and epoxy groups, characteristic of their structure (LIMA et al., 2020). Despite the verification of bands compatible with rGO, the presence of a small number of functional groups in its structure indicates the partial reduction of graphene oxide, once it was observed the presence of bands associated with oxygen groups, such as the epoxy groups (C-O-C) in the band near 1220 cm^{-1} (MEHL et al., 2014). However, the structural differences between graphite, GO and rGO are by the literature and evidence of the successful production of the nanostructures used in this work.

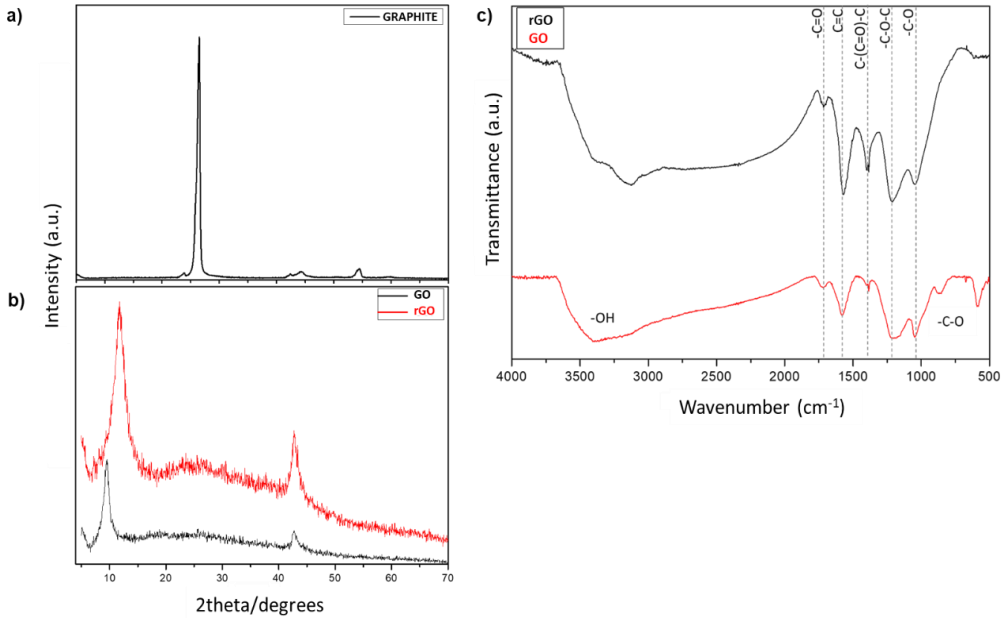

Figure 7. XRD of (a) graphite, (b) GO and rGO (b); (c) FTIR of GO and rGO.

3.2.2 Antimicrobial and Antibiofilm Activities

MIC is defined as the lowest concentration of an antimicrobial agent that inhibits the visible growth of a microorganism (ANDREWS, 2001; DAVIDSON and PARISH, 1989). In this context, MIC for GO and rGO was

not possible, since they did not show antimicrobial activity against the highest priority clinical isolates, *P. aeroginosa* and *MRSA*, even in the highest concentrations tested (2,500 µg/mL). In contrast, against *S. agalactiae*, nanostructures were shown to be effective antimicrobial agents in MIC of 625 µg/mL for GO and 312.5 µg/mL for rGO. From these results, we observed that a lower concentration of rGO is necessary to inhibit the growth of *S. agalactiae* when compared to GO.

Based on this, the antibiofilm capacity was evaluated after 48 h of the nanostructure that showed better antimicrobial activity against *S. agalactiae*. The results of the antibiofilm assay are presented in Figure 8 and demonstrate that, in sub-MIC, rGO can inhibit biofilm formation up to 77%, about positive control.

The ability of rGO to inhibit the biofilm of *S. agalactiae* can be explained by the significant increase of ROS generation and the physical damage caused by its lateral edges to the bacterial cell membranes. Similarly, Guo et al. (2017), showed that rGO in high concentrations was toxic compared to other strains tested, while GO promoted the growth of biofilm. These data are according to Ruiz et al. (2011), where cultures treated with GO at a concentration of 25 µg/mL showed rapid bacterial growth.

In contrast, it was found in the literature that GO coated surfaces are effective against resistant bacteria such as *Escherichia coli* and *P. aeruginosa* (CARPIO et al., 2012; GURUNATHAN, 2012; YADAV et al., 2017). The variability of these studies regarding GO bacterial activity can be explained by cell growth and EPS formation depending on the type of medium, temperature, and type of strain tested (COMBROUSE et al., 2013). Also, the addition of several wash steps during GO can change the pH of acid to neutral and affect the antibacterial activity of GO and rGO (BARBOLINA et al., 2016), which was performed in this work to reduce the biological toxicity of nanoparticles and probably this was the reason for the absence of antimicrobial activity against clinical isolates *P. agalactiae* and MRSA.

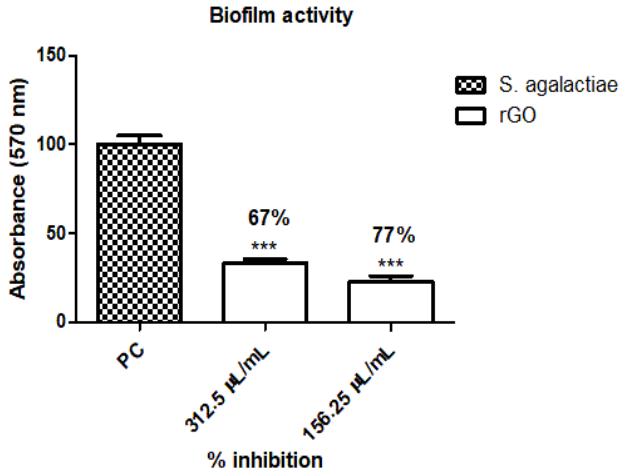

Figure 8. Antibiotic action of rGO in subinhibitory concentration (sub-MIC) in front of strain *S. agalactiae*.

3.2.3 Hemolytic activity

In the toxicity tests, the first 5 concentrations of the serial dilution (2,500, 1,250, 625, 312.5, and 156.25 µg/mL) of GO and rGO were used, which were determined to have antimicrobial activity and antibiofilm previously. The data obtained in this test (Figure 9 a, b, and c) demonstrate that in all the tested pH, the percentage of free hemoglobin in the supernatant of the nanostructures is similar to the negative control,

non-toxic to blood plasma. At pH 7.4 (Fig. 9b), a statistically significant increase in hemolytic activity is noted at the lowest concentration (156.25 µg/mL) of rGO, however, not at the same degree of damage to red blood cells presented by positive control (DMSO).

In the coagulation test, as a reference, the interval between 11 and 15 seconds was used for PT baseline values (Fig. 9d) and the interval between 25 and 35 seconds for APTT normal value (Fig. 9e), according to Salvador-Morales et al. (2009). The time for PT and APTT in all tested concentrations of both treatments remained within the physiological range.

The hemolytic activity of GO and rGO found in this work is following the literature, which demonstrates that graphene-derived nanomaterials are compatible with blood and do not cause hemolysis, alterations in coagulation, or abnormalities in hematological parameters (MENDONÇA, 2016; PINTO and GONÇALVES and MAGALHÃES, 2013).

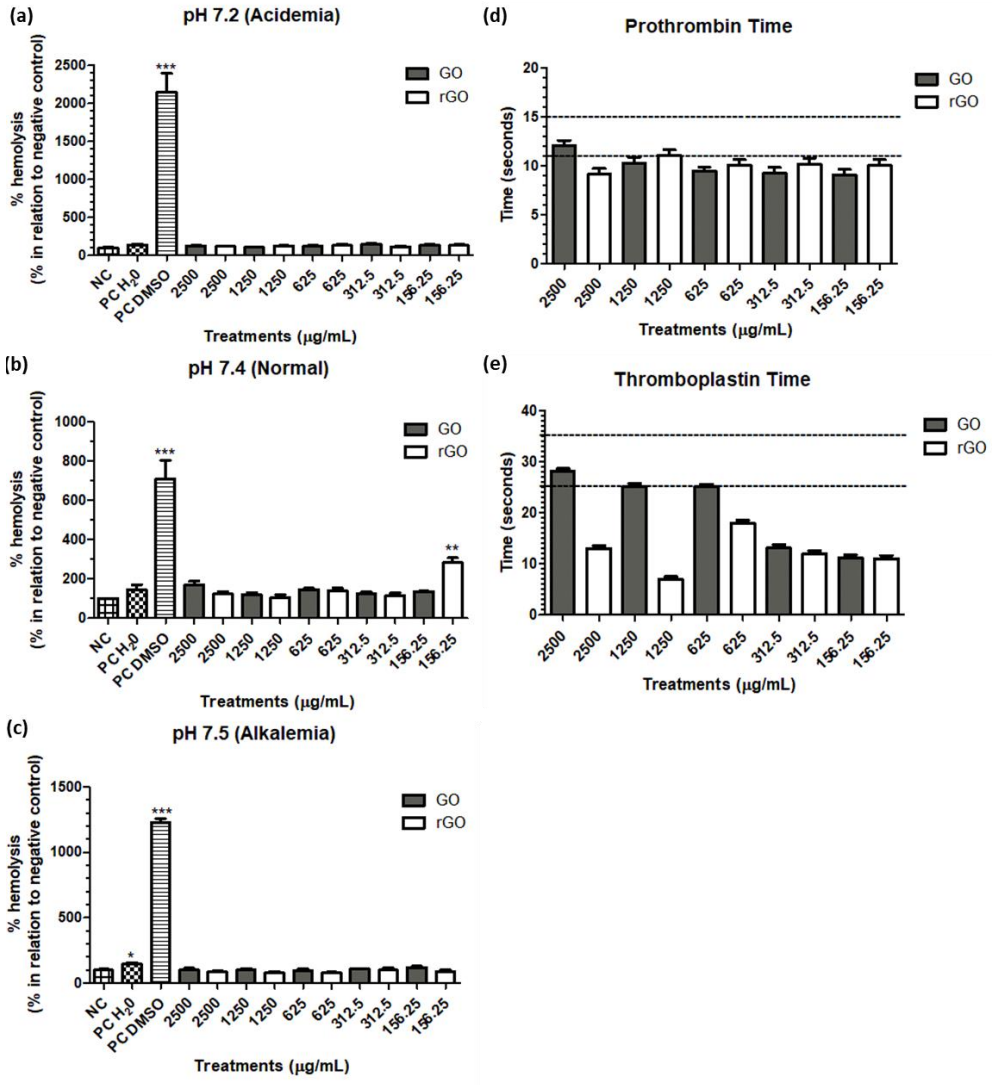

Figure 9. Hemolytic activity of GO and rGO. Hemolysis at pH (a) 7.2, (b) 7.4 (b) and (c) 7.5; (d) Prothrombin Time and (e) The Thromboplastin Time, regarding the coagulation test.

3.2.5 Safety tests

Figure 10 shows the results of MTT, NO, DCFH-DA, and PicoGreen tests, where their NC was composed of cells and culture medium, and in PC the cells were exposed to H_2O_2 (25 and 100 µM), which induced more damage at the highest concentration tested. The data obtained show a significant increase in cell proliferation (Fig. 10a) and the production of DCF (Fig. 10c) at the highest concentrations of GO and rGO. Also, rGO induces significant DNA damage (Fig. 10d) at concentrations of 1,250 and 625 µg/mL, while GO does not. The levels of nitric oxide (Fig. 10b) present in all treated samples were statistically equal to the NC.

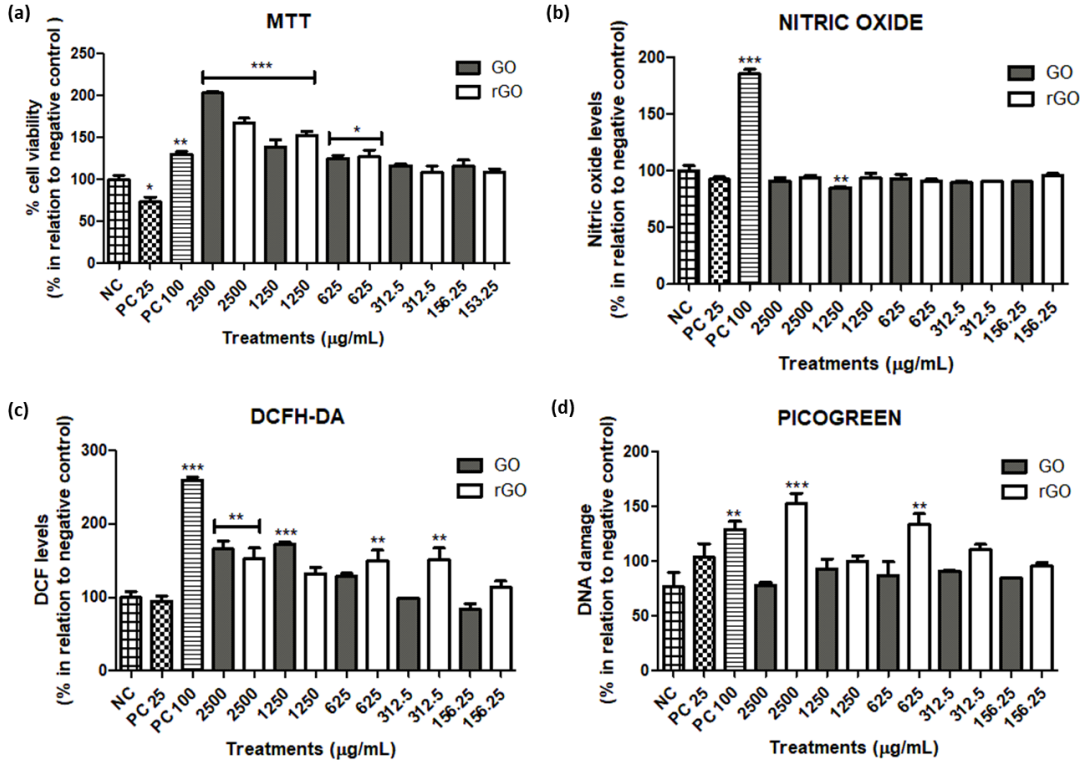

Figure 10. (a) Evaluation of cell viability, (b) NO levels, (c) total DCF levels and, (d) DNA damage in healthy human cells from GO and GOr treatments.

In this study, for the cytotoxic analysis of NPs we prioritized the concentrations that previously presented antimicrobial activity against *S. agalactiae*, that is, 2,500, 1,250, and 625 µg/mL for GO and 2,500, 1,250, 625, and 312.5 µg/mL for rGO. In vitro tests showed that at the three highest concentrations both treatments were not biologically safe, therefore the concentrations of interest of GO were considered toxic. Verifying the efficacy of the antimicrobial activity of MIC of rGO, as well as its biological safety, we chose the concentration of 312,5 µg/mL for the accomplishment of the anti-inflammatory and healing activities in vitro.

An et al. (2018) investigated the ocular toxicity of repeated exposure of GO and rGO nanoparticles in mice, in vitro, and in vivo. The authors reported that short-term GO exposure causes obvious intraocular inflammation, neovascularization of the iris, cell apoptosis in the cornea, and significant cytotoxicity of corneal epithelial cells, while GO does not cause significant eye toxicity. Thus, they concluded that GO is cytotoxic, and this corroborates with the choice of rGO for the continuity of this work.

The best bioactivity of rGO was also found in Kanayama et al. (2014), who analyzed the biological effects of scaffolds implanted in the subcutaneous tissue of the back of a mouse. Among the results found, scaffolds coated with rGO, obtained from the same reducing agent (ascorbic acid) used in this work, presented a tissue growth rate 19% higher than that of structures coated with GO.

3.2.6 Anti-inflammatory activity

PHA mimics inflammation in cell culture by stimulating cell division and metabolic activity (LYU and PARK, 2005) and thus can be used to investigate the anti-inflammatory action of nanomaterials. In this work, the ideal parameters for the tests were determined according to the results of Figure 11a, in which monocytes treated during 48 h with 50 µg/mL of PHA induced cell proliferation and NO levels similar to the damage caused by PC (H_2O_2).

Subsequently, the anti-inflammatory potential of rGO against PHA-induced inflammation was analyzed. In the MTT test (Fig. 11b), it was shown that rGO causes greater cell proliferation than PHA, however, this increase in absorbance may have been influenced by the dark staining of the treatment tested. In Fig. 11b it is also statistically demonstrated that rGO presents NO improving levels at NC and different at PC, thus indicating the anti-inflammatory and non-inflammatory behavior of the nanostructure at a concentration of 312.5 µg/mL.

Mendonça et al. (2016) found that intravenous administration of rGO for seven days did not cause inflammation in rats, as well as no significant change in the expression of inflammatory markers (IL-6, IFN-γ, and TNF-α) in the hippocampus over time. These data are by the in silico and in vitro results obtained in this work, in which rGO NPs do not induce inflammatory indicators, such as excess production of NO and pro-inflammatory cytokines.

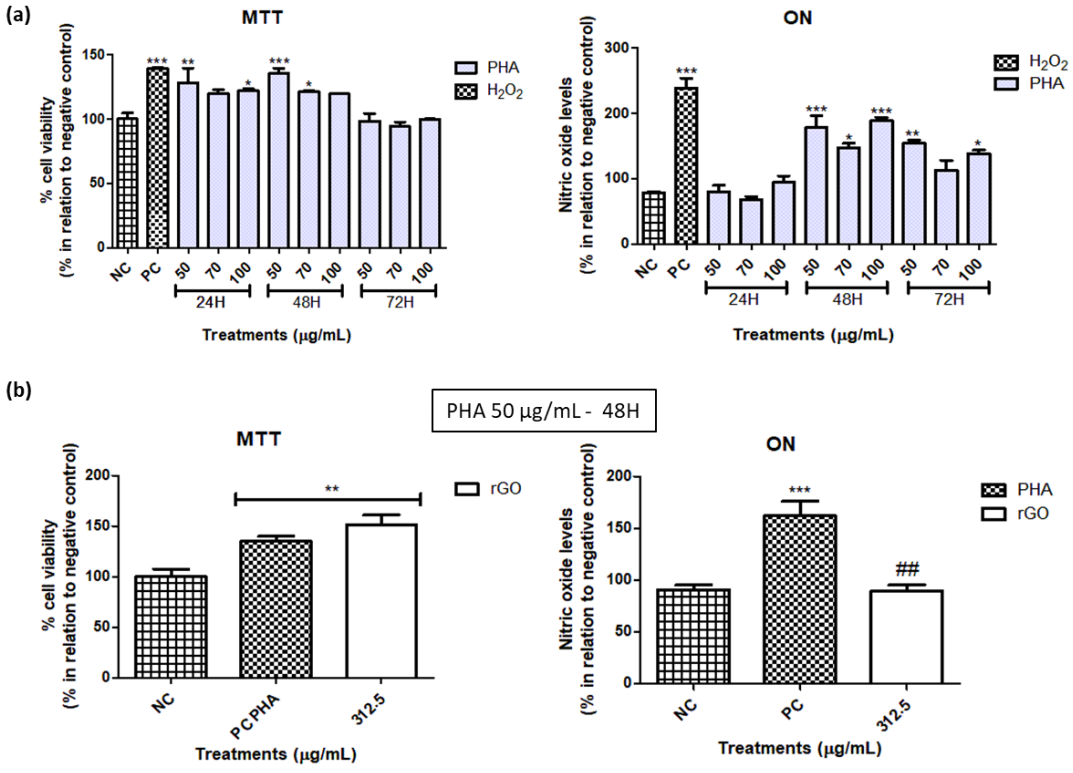

Figure 11. (a) Test curves for the choice of ideal parameters; (b) MTT and NO tests of monocytes treated during 48 h with rGO (312.5 µg/mL) and PHA (50 µg/mL).

3.2.7 Scratch assay

Micrographs of healthy fibroblast cells and after cutting are shown in Figure 12a. In samples containing rGO, black dots of agglomerations are observed indicating that the treatment was not fully solubilized, which was expected due to its known hydrophobic behavior.

The healing process of treated and untreated samples was followed for 48 h, and the images referring to the final time are presented in Figure 12b. It is noted the occurrence of migration of the cells into the lesion in all samples, however, the protruding lines at the cut edges make a qualitative analysis of the images impossible, as they represent that the culture plate was scratched during the Scratch assay, possibly due to excessive force applied to the needle.

Since samples from NC and supernatant treatment facilitate the visualization of cells, they were chosen for quantitative analysis of the percentage of cells present at the site of injury after 48 h. The results concerning the analysis of the images are presented in Fig. 12c and Table 4. Based on this, it is verified that the treatment with rGO (312.5 µg/mL) increases on average 21.2% the migration of cells in the lesion when compared to the NC, and thus it is verified that the nanostructure accelerates the process of wound healing in vitro.

In the literature, when used as dressings, nanocomposites of rGO and polymers promote an acceleration in wound contraction (QIAN et al., 2018; THANGAVEL et al, 2018). However, studies related to the healing properties of pure rGO NPs were not found. Therefore, this is the first work that demonstrates healing activity or cellular migration of pure rGO, verified through scripting in Python programming language.

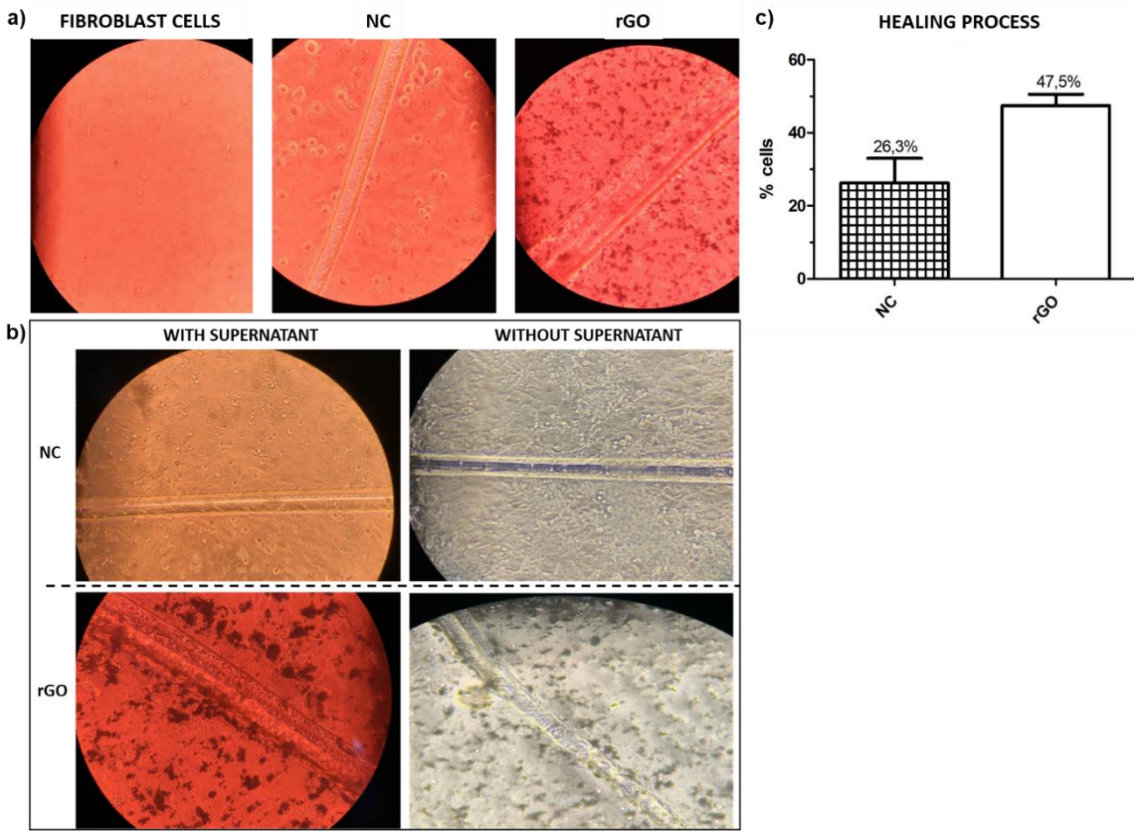

Figure 12. (a) Microscopy images of fibroblast cells before cutting and NC and rGO samples at the time of cutting; (b) Microscopy images of the healing process of NC and rGO 48H samples after cutting; (c) Percentage of cells present at the lesion site after 48H, in samples with (GOr) and without treatment (NC), according to data in Table 4.

Table 4. Results regarding image analysis of samples (without supernatant) of NC and rGO, after 48H of cutting. Data obtained through a script in Python programming language.

ARCHIVE	CELL	NON-CELL	TOTAL CELLS	% CELL	% NON-CELLS
NC (sample1)	8453	54047	62500	13,5248	86,4752
NC (sample2)	18050	44450	62500	28,88	71,12
NC (sample3)	22776	39724	62500	36,4416	63,5584
rGO (sample1)	29315	33185	62500	46,904	53,096
rGO (sample2)	33195	29305	62500	53,112	46,888
rGO (sample3)	26544	35956	62500	42,4704	57,5296

3. CONCLUSION

Although this is a preliminary study, which requires further clinical trials and evidence, the results presented here allow us to infer that pure rGO can be a strong candidate for applications in the treatment of chronic wounds, because it has proven to be biologically safe and has good antimicrobial, anti-inflammatory, and healing properties. From a future perspective, it is expected that studies related to cytokines will be carried out, to confirm the in silico results of this work. Moreover, it will be interesting

the accomplishment of studies relating rGO with antimicrobials frequently used in the treatments of wounds and incorporations of this NP in topical formulations of antibacterial agents and dressings with controlled release.

4. ACKNOWLEDGMENT

This work was carried out with the support of the Coordination for the Improvement of Higher Education Personnel - Brazil (CAPES) - Financing Code 001. The authors wish to thank the Franciscan University and the Centro Nacional de Processamento de Alto Desempenho (CENAPAD) from São Paulo for the computational space.

5. REFERENCES

P.C. Adamson. et al. Variability in the oral bioavailability of all-trans-retinoic acid. J Natl Cancer Inst. 1993; 85(12): 993-996. https://doi.org/10.1093/jnci/85.12.993

R.S. Ambekar, and B. Kandasubramanian. A polydopamine-based platform for anti-cancer drug delivery. Biomater. Sci. 2019; 7: 1776-1793. https://doi.org/10.1039/C8BM01642A

W. An. et al. Ocular toxicity of reduced graphene oxide or graphene oxide exposure in mouse eyes. Experimental Eye Research. 2018; 174: 59-69. https://doi.org/10.1016/j.exer.2018.05.024

J.M. Andrews. Determination of minimum inhibitory concentrations. The Journal of Antimicrobial Chemotherapy. 2001; 48(1): 5-16. https://doi.org/10.1093/jac/48.suppl_1.5

B.A. Avelar. et al. The crude latex of Euphorbia tirucalli modulates the cytokine response of leukocytes, especially CD4+ T lymphocytes. Rev. Bras. Farmacogn. 2011; 21(4): 662-667. https://doi.org/10.1590/S0102-695X2011005000096

I. Barbolina. et al. Purity of graphene oxide determines its antibacterial activity. 2D Materials. 2016; 3(2): e25025. https://doi.org/10.1088/2053-1583/3/2/025025

H.M. Bermam. et al. The protein data bank. Nucleic Acids Research. 2000; 28(1). https://doi.org/10.1093/nar/28.1.235

T. Bjarnsholt. The role of bacterial biofilms in chronic infections. APMIS. 2013; 121(136): 1-54. https://doi.org/10.1111/apm.12099

P. Capelari-Oliveira. et al. Anti-inflammatory activity of Lychnophora passerina, Asteraceae (Brazilian “Arnica”). Journal of Ethnopharmacology. 2011; 135(2): 393-39. https://doi.org/10.1016/j.jep.2011.03.034

I.E.M. Carpio. et al. Toxicity of a polymer–graphene oxide composite against bacterial planktonic cells, biofilms, and mammalian cells. Nanoscale. 2012; 4(15): 4746-4756, 2012. https://doi.org/10.1039/C2NR30774J

D.R. Childs, and A.S. Murthy. Overview of Wound Healing and Management. Surgical Clinics of North America. 2018; 97(1): 189-207. https://doi.org/10.1016/j.suc.2016.08.013

N. Chiu, T. Huang, and H. Lai. Graphene oxide based surface plasmon resonance biosensors. Advances in Graphene Science. 2013; p. 191-216. https://doi.org/10.5772/56221

C.K. Chua, and M. Pumera. Chemical reduction of graphene oxide: a synthetic chemistry viewpoint. Chemical Society Reviews. 2014; 43: 291-312. https://doi.org/10.1039/C3CS60303B

C. Chung. et al. Biomedical applications of graphene and graphene oxide. Accounts of Chemical Research. 2013; 46(10): 2211-2224. https://doi.org/10.1021/ar300159f

T. Combrouse. et al. Quantification of the extracellular matrix of the Listeria monocytogenes biofilms of different phylogenic lineages with optimization of culture conditions. J. Appl. Microbiol. 2013; 114: 1120-1131. https://doi.org/10.1111/jam.12127

G.L. Cordeiro. Síntese e processamento de óxido de grafeno reduzido: Abordagens no desenvolvimento de eletrocatalisadores suportados para oxidação de etanol. 2018. 121 p. Tese (Doutorado em Tecnologia Nuclear) – Instituto de Pesquisas Energéticas e Nucleares – IPENCNEN/SP, São Paulo, 2018.

F.J. Cossetin. et al. Peanut leaf extract has antioxidant and anti-inflammatory activity but no acute toxic effects. Regulatory Toxicology and Pharmacology. 2019; 107: e104407. https://doi.org/10.1016/j.yrtph.2019.104407

P.M. Davidson, and M.E. Parish. Methods for testing the efficacy of food antimicrobials. Food Technol. 1989; 43: 148-155.

H. Derakhshandeh. et al. Smart bandages: the future of wound care. Trends in Biotechnology. 2018; 36(12): 1259-1274. https://doi.org/10.1016/j.tibtech.2018.07.007

R. Diez-Orejas.et al. Graphene oxide nanosheets increase Candida albicans killing by pro-inflammatory and reparative peritoneal macrophages. Colloids and Surfaces B: Biointerfaces. 2018; 171: 250-259. https://doi.org/10.1016/j.colsurfb.2018.07.027

M.A. Dobrovolskaia. et al. Interaction of colloidal gold nanoparticles with human blood: effects on particle size and analysis of plasma protein binding profiles. Nanomedicine. 2009; 5: 106-117. https://doi.org/10.1016/j.nano.2008.08.001

R.M. Donlan and J.W. Costerton. Biofilms: survival mechanisms of clinically relevant microorganisms. Clin. Microbiol. Rev. 2002; 15: 167-193. https://doi.org/10.1128/CMR.15.2.167-193.2002

D. Dorfey, S.R. Mortari, and T.M. Volkmer. Synthesis and characterization of Graphene oxide and reduced graphene oxide. Disciplinarum Scientia. Série: Naturais e Tecnológicas, Santa Maria. 2017; 18(3): 421-432.

M.G. Durruthy. et al. Decrypting Strong and Weak Single-Walled Carbon Nanotubes Interactions with Mitochondrial Voltage-Dependent Anion Channels Using Molecular Docking and Perturbation Theory. Nature Scientific Reports. 2017; 7(1): 1-19. https://doi.org/10.1038/s41598-017-13691-8

H. Fallatah. et al. Antibacterial effect of graphene oxide (GO) nanoparticles against Pseudomonas putida biofilm of variable age. Environ. Sci. Pollut Res. 2019; 26: 25057-25070. https://doi.org/10.1007/s11356-019-05688-9

G.S. Faria. et al. Produção e caracterização de óxido de grafeno e óxido de grafeno reduzido com diferentes tempos de oxidação. Matéria (Rio J.). 2017; 22(1): e11918. https://doi.org/10.1590/S1517-707620170005.0254

W.P. Feinstein, and M. Brylinski. Calculating an optimal box size for ligand docking and virtual screening against experimental and predicted binding pockets. J. Cheminform. 2015; 7(18). https://doi.org/10.1186/s13321-015-0067-5

S. Forli. et al. Computational protein–ligand docking and virtual drug screening with the AutoDock suite. Nat. Protoc. 2016; 11: 905-919. https://doi.org/10.1038/nprot.2016.051

A. Grada. et al. Research Techniques Made Simple: Analysis of Collective Cell Migration Using the Wound Healing Assay. Journal of Investigative Dermatology. 2017; 137(2): 11-16. https://doi.org/10.1016/j.jid.2016.11.020

Z. Guo. et al. Toxicity and transformation of graphene oxide and reduced graphene oxide in bacteria biofilm. Science of The Total Environment. 2017; 580: 1300-1308. https://doi.org/10.1016/j.scitotenv.2016.12.093

S. Gurunathan. et al. Oxidative stress-mediated antibacterial activity of graphene oxide and reduced graphene oxide in Pseudomonas aeruginosa. Int. J. Nanomedicine. 2012; 7: 5901-5914. https://doi.org/10.2147/IJN.S37397

W.S. Hummers, and R.E. Offeman. Preparation of Graphitic Oxide. Journal of the American Chemical Society. 1958; 80(6): 1339. https://doi.org/10.1021/ja01539a017

E. Jiménez. et al. Synthesis, Biological Evaluation and Molecular Docking of New Benzenesulfonylhydrazone as Potential anti-Trypanosoma cruzi Agents. Med. Chem. 2017; 13(2): 149-158. https://doi.org/10.2174/1573406412666160701022230

I. Kanayama. et al. Comparative study of bioactivity of collagen scaffolds coated with graphene oxide and reduced graphene oxide. Int. J. Nanomedicine. 2014; 11(9): 3363-3373. https://doi.org/10.2147/IJN.S62342

B.H. Kim. et al. Anatomy of high recyclability of graphene oxide based palladium nanocomposites in the Sonogashira reaction: On the nature of the catalyst deactivation. Mater. Express. 2016; 6: 61-68. https://doi.org/10.1166/mex.2016.1280

K. Krishnamoorthy. et al. The chemical and structural analysis of graphene oxide with different degrees of oxidation. Carbon. 2013; 53: 38-49. https://doi.org/10.1016/j.carbon.2012.10.013

T. Kuila. et al. Recent advances in the efficient reduction of graphene oxide and its application as energy storage electrode materials. Nanoscale. 2013; 5: 52-71. https://doi.org/10.1039/C2NR32703A

R.A. Laskowski, and M.B. Swindells. LigPlot+: Multiple ligand-protein interaction diagrams for drug discovery. Journal of Chemical Information and Modeling. 2011; 51(10): 2778-2786. https://doi.org/10.1021/ci200227u

L.R.M. Lima. et al. Characterization of commercial graphene-based materials for application in thermoplastic nanocomposites. Materials Today: Proceedings. 2020; 20(3): 383-390. https://doi.org/10.1016/j.matpr.2019.10.077

S.Y. Lyu, and W.B. Park. Production of cytokine and NO by RAW 264.7 macrophages and PBMC in vitro incubation with flavonoids. Arch. Pharm. Res. 2005; 28(5): 573-581. https://doi.org/10.1007/BF02977761

M. Maczynski. et al. Anti-inflammatory properties of na isoxazole derivative – MZO-2. Pharmacological Reports. 2008; 68: 894 - 902. https://doi.org/10.1016/j.pharep.2016.04.017

C.T.M. Mascio, J.D. Alder, and J.A. Silverman. Bactericidal action of daptomycin against stationary- phase and nondividing Staphylococcus aureus cells. Antimicrob Agents Chemother. 2007; 51(12): 4255-4260. https://doi.org/10.1128/AAC.00824-07

H. Mehl. et al. Efeito da variação de parâmetros reacionais na preparação de grafeno via oxidação e redução do grafite. Química Nova. 2014; 37(10): 1639-1645. https://doi.org/10.5935/0100-4042.20140252

M.C.P. Mendonça. et al. Reduced graphene oxide: nanotoxicological profile in rats. J Nanobiotechnol. 2016; 14(53). https://doi.org/10.1186/s12951-016-0206-9

R.D. Monds, and G.A. O'Toole The developmental model of microbial biofilms: ten years of a paradigm up for review. Trends Microbiol. 2009; 17: 73-87. https://doi.org/10.1016/j.tim.2008.11.001

T. Mosmann. Rapid colorimetric assay for cellular growth and survival: application to proliferation and cytotoxicity assays. Journal Of Immunological Methods. 1983; 65(1-2): 55-63. https://doi.org/10.1016/0022-1759(83)90303-4

V.S.K. Nishihira. et al. In vitro and in silico protein corona formation evaluation of curcumin and capsaicin loaded-solid lipid nanoparticles. Toxicology in Vitro. 2019; 61: e104598. https://doi.org/10.1016/j.tiv.2019.104598

A.M. Pinto, I.C. Gonçalves, and F.D. Magalhães. Graphene-based materials biocompatibility: A review. Colloids and Surfaces B: Biointerfaces. 2013; 111: 188-202. https://doi.org/10.1016/j.colsurfb.2013.05.022

K.C. Preethi, G. Kuttan, and R. Kuttan. Anti-inflammatory activity of flower extract of Calendula officinalis Linn. and its possible mechanism of action. Indian J Exp Biol. 2009; 47(2): 113-20.

W. Qian. et al. Polydimethylsiloxane incorporated with reduced graphene oxide (rGO) sheets for wound dressing application: Preparation and characterization. Colloids and Surfaces B: Biointerfaces, v. 166, p. 61-71, 2018. https://doi.org/10.1016/j.colsurfb.2018.03.008

Y. Qin. Antimicrobial textile dressings to manage wound infection. Advanced Textiles for Wound Care (2 ed.), In: The Textile Institute Book Series. 2019; 193-210. https://doi.org/10.1533/9781845696306.1.179

H. Reinecke. et al. Peripheral arterial disease and critical limb ischaemia: Still poor outcomes and lack of guideline adherence. European Heart Journal. 2015; 36(15): 932-938. https://doi.org/10.1093/eurheartj/ehv006

R.C. Riéffel. Desenvolvimento e avaliação farmacológica in vitro de nanocápsulas contendo óleo de Astrocaryum vulgare no reparo tecidual cutâneo. 2019. Dissertação de mestrado – Universidade Franciscana, Programa de Pós-Graduação em Nanociências, RS, 2019.

H.J.J. Rosas. et al. First principles calculations of the electronic and chemical properties of graphene, graphane, and graphene oxide. J. Mol. Model. 2011; 17:1133-1139. https://doi.org/10.1007/s00894-010-0818-1

A. Rossato. et al. Evaluation in vitro of antimicrobial activity of tucumã oil (Astrocaryum Vulgare). Archives in Biosciences & Health. 2019; 1(1): 99-112. https://doi.org/10.18593/abh.19701

O.N. Ruiz. et al. Graphene oxide: a nonspecific enhancer of cellular growth. ACS Nano. 2011; 5(10): 8100-8107. https://doi.org/10.1021/nn202699t

M.R. Sagrillo. et al. Tucumã fruit extracts (Astrocaryum aculeatum Meyer) decrease cytotoxic effects of hydrogen peroxide on human lymphocytes. Food Chemistry. 2015; 173:741–748. https://doi.org/10.1016/j.foodchem.2014.10.067

C. Salvador-Morales. et al. Immunocompatibility properties of lipid–polymer hybrid nanoparticles with heterogeneous surface functional groups. Biomaterials. 2009; 30: 2231-2240. https://doi.org/10.1016/j.biomaterials.2009.01.005

J. Shen. et al. Fast and facile preparation of graphene oxide and reduced graphene. Chem. Mater. 2009; 21: 3514-3520. https://doi.org/10.1021/cm901247t

R. Siburian. et al. New Route to Synthesize of Graphene Nano Sheets. Oriental Journal of Chemistry. 2018; 34(1):182-187. http://dx.doi.org/10.13005/ojc/340120

K.K.H. Silva, H. Huang, and M. Yoshimura. Progress of reduction of graphene oxide by ascorbic acid. Applied Surface Science. 2018; 447: 338-346. https://doi.org/10.1016/j.apsusc.2018.03.243

D.P. Singh. et al. Graphene oxide: An efficient material and recent approach for biotechnological and biomedical applications. Materials Science and Engineering C. 2018; 86: 173-197. https://doi.org/10.1016/j.msec.2018.01.004

P. Smaniotto. et al. Tratamento clínico das feridas - curativos. Rev Med (São Paulo). 2010; 89(3/4): 137-141. https://doi.org/10.11606/issn.1679-9836.v89i3/4p137-141

A.E.S. Sousa. et al. O papel da arginina e glutamina na imunomodulação em pacientes queimados - revisão de literatura. Rev. Bras. Queimaduras. 2015;14(4): 295-299.

S. Stepanović. et al. Quantification of biofilm in microtiter plates: overview of testing conditions and practical recommendations for assessment of biofilm production by staphylococci. APMIS. 2007; 115(8): 891-899. https://doi.org/10.1111/j.1600-0463.2007.apm_630.x

X. Sun. et al. Nano-graphene oxide for cellular imaging and drug delivery. Nano research. 2008; 1(3): 203-212. https://doi.org/10.1007/s12274-008-8021-8

S. Thampi. et al. Differential Adhesive and Bioactive Properties of the Polymeric Surface Coated with Graphene Oxide Thin Film. ACS Applied Materials and Interfaces. 2017; 9(5): 4498-4508. https://doi.org/10.1021/acsami.6b14863

P. Thangavel. et al. Development of reduced graphene oxide (rGO)-isabgol nanocomposite dressings for enhanced vascularization and accelerated wound healing in normal and diabetic rats. Journal of Colloid and Interface Science. 2018; 517: 251-264. https://doi.org/10.1016/j.jcis.2018.01.110

O. Trott, and A.J. Olson. AutoDock Vina: Improving the Speed and Accuracy of Docking with a New Scoring Function, Efficient Optimization, and Multithreading. International Journal of Clinical and Experimental Pathology. 2009; 31(2):455-461. https://doi.org/10.1002/jcc.21334

J. Wang, Z. Chen, and B. Chen. Adsorption of Polycyclic Aromatic Hydrocarbons by Graphene and Graphene Oxide Nanosheets. Environmental science & technology. 2014; 48(9): 4817-4825. https://doi.org/10.1021/es405227u

J. Wang, E.C. Salihi, and L. Šiller. Green reduction of graphene oxide using alanine. Materials Science and Engineering C. 2017; 72(1): 1-6. https://doi.org/10.1016/j.msec.2016.11.017

N. Yadav. et al. Graphene oxide- coated surface: inhibition of bacterial biofilm formation due to specific surface–interface interactions. ACS Omega. 2017; 2(7): 3070-3082. https://doi.org/10.1021/acsomega.7b00371

Y. Yang. et al. Graphene based materials for biomedical applications. Materials Today. 2013; 16(10): 365-373. https://doi.org/10.1016/j.mattod.2013.09.004

R. Zine, and M. Sinha. Nanofibrous poly (3-hydroxybutyrate-co-3 hydroxyvalerate)/collagen/ graphene oxide scaffolds for wound coverage. Materials Science & Engineering C. 2017; 80: 129-134. https://doi.org/10.1016/j.msec.2017.05.138